

# Origin of multiwavelength emission from flaring high redshift blazar PKS 0537-286

N. Sahakyan<sup>1,2,3</sup>, <sup>★</sup> G. Harutyunyan<sup>1,4</sup>, D. Israyelyan<sup>1</sup>

<sup>1</sup>ICRANet-Armenia, Marshall Baghramian Avenue 24a, Yerevan 0019, Armenia

<sup>2</sup>ICRANet, P.zza della Repubblica 10, 65122 Pescara, Italy

<sup>3</sup>ICRA, Dipartimento di Fisica, Sapienza Università di Roma, P.le Aldo Moro 5, 00185 Rome, Italy

<sup>4</sup>Byurakan Astrophysical Observatory, Aragatsotn reg., Armenia

Accepted XXX. Received YYY; in original form ZZZ

## ABSTRACT

The high redshift blazars powered by supermassive black holes with masses exceeding  $10^9 M_\odot$  have the highest jet power and luminosity and are important probes to test the physics of relativistic jets at the early epochs of the Universe. We present a multi-frequency spectral and temporal study of high redshift blazar PKS 0537-286 by analyzing data from *Fermi*-LAT, NuSTAR Swift XRT and UVOT. Although the time averaged  $\gamma$ -ray spectrum of the source is relatively soft (indicating the high-energy emission peak is below the GeV range), several prominent flares were observed when the spectrum hardened and the luminosity increased above  $10^{49} \text{ erg s}^{-1}$ . The X-ray emission of the source varies in different observations and is characterised by a hard spectrum  $\leq 1.38$  with a luminosity of  $> 10^{47} \text{ erg s}^{-1}$ . The broadband spectral energy distribution in the quiescent and flaring periods was modeled within a one-zone leptonic scenario assuming different locations of the emission region and considering both internal (synchrotron radiation) and external (from the disk, broad-line region and dusty torus) photon fields for the inverse Compton scattering. The modeling shows that the most optimistic scenario, from the energy requirement point of view, is when the jet energy dissipation occurs within the broad-line region. The comparison of the model parameters obtained for the quiescent and flaring periods suggests that the flaring activities are most likely caused by the hardening of the emitting electron spectral index and shifting of the cut-off energy to higher values.

**Key words:** galaxies: jets – galaxies: active – gamma-rays: galaxies – quasars: individual: PKS 0537-286

## 1 INTRODUCTION

Blazars are radio-loud quasars with powerful relativistic jets that make a small angle to the observer’s line of sight (Urry & Padovani 1995). They are among the most energetic sources in the Universe and a dominant class of extragalactic sources in the high energy (HE;  $> 100 \text{ MeV}$ )  $\gamma$ -ray sky (e.g., Abdollahi et al. 2022). The new possibility of extensive multiwavelength observations coupled with multi-messenger observations have the potential to widen our understanding of blazars.

Historically, blazars are sub-grouped in two large sub-classes: BL Lacs and flat-spectrum radio quasars (FSRQs) (Urry & Padovani 1995). BL Lacs have nearly featureless optical spectra (very weak or no lines are observed) while the FSRQs have bright and broad lines with equivalent widths of  $|\text{EM}| > 5 \text{ \AA}$ . One of the most distinguishable features of blazars is the very strong variability of their emission in almost all the observed bands in various times scales, from minute to week or month scales; (e.g., Arlen et al. 2013; Aleksić et al. 2014; Ackermann et al. 2016; Shukla et al. 2018; Meyer et al. 2019). This variability is stochastic in nature but a recent detection of quasi-periodic oscillations was reported (e.g., see Peñil et al. 2020; Ren et al. 2022).

Being powerful emitters, blazars are frequently monitored in all the accessible wavelengths which resulted in accumulation of a substantial amount of data. The emission from blazars, predominantly of a nonthermal nature (e.g., Padovani et al. 2017), is dominated by Doppler-amplified emission from the jet, typically showing two broad peaks: the first at radio to X-ray bands, and the second at  $\gamma$ -rays. The low-energy component peak ( $\nu_{\text{syn}}^{\text{p}}$ ) is used to further classify blazars as low- (LBL/LSP), intermediate- (IBL/ISP) or high- (HBL/HSP) peaked sources when  $\nu_{\text{syn}}^{\text{p}} < 10^{14} \text{ Hz}$ ,  $10^{14} \text{ Hz} < \nu_{\text{syn}}^{\text{p}} < 10^{15}$  and  $\nu_{\text{syn}}^{\text{p}} > 10^{15} \text{ Hz}$ , respectively (Padovani & Giommi 1995; Abdo et al. 2010c). However,  $\nu_{\text{syn}}^{\text{p}}$  can be well above  $2.4 \times 10^{17}$  in extreme blazars (e.g., Giommi et al. 1999; Costamante et al. 2001; Bêteau et al. 2020; Pian et al. 1998; Sahakyan 2020) which are interesting as they challenge our current understanding of particle acceleration and emission processes. In addition, the remarkable  $\gamma$ -ray blazar 4FGL J1544.3-0649, which was undetected in the X-ray and  $\gamma$ -rays until May 2017, showed a transient-like behaviour, becoming a very bright source for a few months and detected by Fermi Large Area telescope (*Fermi*-LAT) and MAXI X-ray sky monitor (Sahakyan & Giommi 2021). This suggests the existence of an undiscovered blazar population which may occasionally flare.

The broadband spectral energy distribution (SED) of blazars can be modeled within different scenarios involving the interaction of electrons and protons in a single or multiple zone. Although, there is

<sup>★</sup> E-mail: narek@icra.it

a consensus that the low-energy component is due to the synchrotron emission of ultra-relativistic charged electrons in the blazar jet, the origin of the second component is highly debated. In the leptonic scenarios, this component is due to inverse Compton scattering of low-energy photons which might be the produced synchrotron photons (synchrotron-self Compton model, SSC; [Ghisellini et al. 1985](#); [Maraschi et al. 1992](#); [Bloom & Marscher 1996](#)) or be of an external origin (e.g., [Sikora et al. 1994](#)), such as photons directly emitted from the accretion disk ([Dermer et al. 1992](#); [Dermer & Schlickeiser 1994](#)) or reflected from the broad-line region ([Sikora et al. 1994](#)) or emitted from the dusty torus ([Błażejowski et al. 2000](#)). Alternatively, the second component can be due to either the synchrotron emission of the energetic protons inside the jet ([Mücke & Protheroe 2001](#)) or due to the secondaries generated in photo-pion and photo-pair interactions ([Mannheim 1993](#); [Mannheim & Biermann 1989](#); [Mücke & Protheroe 2001](#); [Mücke et al. 2003](#); [Böttcher et al. 2013](#); [Petropoulou & Mastichiadis 2015](#); [Gasparyan et al. 2022](#)). These hadronic models (especially lepto-hadronic models, e.g., [Ansoldi et al. 2018](#); [Keivani et al. 2018](#); [Murase et al. 2018](#); [Padovani et al. 2018](#); [Sahakyan 2018](#); [Righi et al. 2019](#); [Cerruti et al. 2019](#); [Sahakyan 2019](#); [Gao et al. 2019](#); [Gasparyan et al. 2022](#)) have become more attractive after the observations of IceCube-170922A neutrino event from the direction of TXS 0506+056 ([IceCube Collaboration et al. 2018a,b](#); [Padovani et al. 2018](#)) as well as after the observations of multiple neutrino events from the direction of PKS 0735+178 when it was bright in the optical/UV, X-ray and  $\gamma$ -ray bands ([Sahakyan et al. 2022a](#)).

Due to the extreme luminosities of blazars, even very high redshift ones can be observed (e.g., see [Ackermann et al. 2017](#)). The observation of distant blazars is of particular interest as they allow i) to study the relativistic jets as well as their connection with accretion disk/black hole in the early epochs of the Universe, ii) to measure the suppression of the  $\gamma$ -ray flux which can be used to estimate or constraint the density of the extragalactic background light (EBL) ([Kneiske et al. 2004](#); [Mazin & Raue 2007](#); [Franceschini et al. 2008](#)) and understand its cosmological evolution, iii) to investigate, in general, the properties of  $\gamma$ -ray emitting active galactic nuclei (AGN), which is important for the understanding of the cosmological evolution of the  $\gamma$ -ray background ([Abdo et al. 2010a](#)).

Due to their faintness, high redshift blazars are rather difficult to observe and identify, limiting the number of already associated high redshift blazars. For example, in the fourth catalog of AGNs detected by *Fermi*-LAT (data release 3 (DR3); [Abdollahi et al. 2022](#)) only 110 blazars are observed beyond  $z = 2.0$  and only 10 beyond  $z = 3.0$ . The most distant blazar observed in the  $\gamma$ -ray band is GB1508+5714 at  $z = 4.31$ . The physical properties of these high redshift blazars have been frequently investigated using multi-frequency data (e.g., [Ghisellini et al. 2009, 2011](#); [Paliya 2015](#); [Paliya et al. 2016](#); [Marcotulli et al. 2017](#); [Ackermann et al. 2017](#); [Li et al. 2018](#); [Paliya et al. 2019](#)). For example, in [Paliya et al. \(2020\)](#) by studying nine  $\gamma$ -ray emitting blazars and 133 candidate blazars with soft X-ray spectra it is shown that these high redshift blazars host massive black holes ( $M_{\text{BH}} > 10^9 M_{\odot}$ ) and have an accretion disk luminosity of  $> 10^{46} \text{ erg s}^{-1}$ . Or, in [Sahakyan et al. \(2020b\)](#), by studying the spectral and temporal properties of thirty-three distant blazars ( $z > 2.5$ ) and modeling their SEDs, it is found that the emission region size is  $\leq 0.05 \text{ pc}$ , while the magnetic field and the Doppler factor are correspondingly within  $0.10 - 1.74 \text{ G}$  and  $10.0 - 27.4$ .

Although the number of observed high redshift blazars is not high enough to perform statistically sound population studies, the investigation of the properties of individual objects provides interesting peaces to understand the general physics of high redshift blazars. The multiwavelength monitoring of several high redshift blazars opens

wide opportunities for investigation of their multiwavelength spectral and temporal properties as well as for performing detailed theoretical modeling and interpretation of the results. For example, the continuous monitoring of these sources in the HE  $\gamma$ -ray band by *Fermi*-LAT ([Atwood et al. 2009](#)) allows to select various emission states, or their observations in the X-ray band with Neil Gehrels Swift Observatory ([Gehrels et al. 2004](#), hereafter Swift), and Nuclear Spectroscopic Telescope Array (NuSTAR; [Harrison et al. 2013](#)) combined with the  $\gamma$ -ray data allows a precise estimation of the second emission component peak, or the data in the optical/UV bands can be used to constrain the high energy tail of the synchrotron component and/or the direct thermal emission from the accretion disk ([Ghisellini et al. 2011](#)). Therefore, the data available in different bands can be used to put tighter constraints on the physics of individual high redshift blazars.

Here we present a broadband study of PKS 0537-286; at  $z = 3.10$  ([Wright et al. 1978](#)) it is one of the brightest high redshift blazars. It was observed in the X-ray band with various instruments (e.g., Einstein observatory ([Zamorani et al. 1981](#)), ASCA ([Cappi et al. 1997](#); [Siebert et al. 1996](#)), ROSAT ([Fiore et al. 1998](#)), etc.) showing a particularly hard X-ray spectrum ( $\sim 1.2$ ). In the  $\gamma$ -ray band, with an energy flux of  $(1.44 \pm 0.006) \times 10^{-11} \text{ erg cm}^{-2} \text{ s}^{-1}$  in the fourth catalog of *Fermi*-LAT AGNs (DR3; [Abdollahi et al. 2022](#)), it is the brightest blazar beyond  $z = 3.0$ . Moreover, in several occasions  $\gamma$ -ray flares were observed when the daily flux was above  $10^{-6} \text{ photon cm}^{-2} \text{ s}^{-1}$  ([Valverde & Forman 2022](#); [Angioni 2020](#); [Cheung 2017](#)) which makes PKS 0537-286 the most distant  $\gamma$ -ray flaring blazar ([Li et al. 2018](#); [Sahakyan et al. 2020a](#)). The broadband emission from PKS 0537-286 was successfully modeled within a one-zone synchrotron and external inverse Compton scenario where the excess in optical/UV band was interpreted as emission from bright thermal accretion disk ([Bottacini et al. 2010](#)).

In general, the peak of the second component in the SED of high redshift blazars is at MeV energies, which implies their HE  $\gamma$ -ray spectrum is soft, so they are not ideal sources for  $\gamma$ -ray observations. Therefore, the observation of the  $\gamma$ -ray flaring activity of distant blazars, which is crucial for testing different emission scenarios of relativistic jets, is even more interesting as compared with that of the nearby sources. Motivated i) by the availability of multiwavelength data from PKS 0537-286 observations - since 2008 in the HE  $\gamma$ -ray band by *Fermi*-LAT, multiple observations of PKS 0537-286 by Swift X-Ray Telescope (XRT) and Ultra-violet Optical Telescope (UVOT) instruments and two observations of PKS 0537-286 with NuSTAR, and ii) by the observed multiple flaring activities of PKS 0537-286, we decided to investigate the spectral and temporal properties of PKS 0537-286 by analyzing the data accumulated in the optical/UV, X-ray and  $\gamma$ -ray bands and put, through theoretical modeling, a constraint on the physical processes responsible for the PKS 0537-286 emission in the quiescent and flaring states.

The paper is structured as follows. The data extraction and analysis in the  $\gamma$ -ray, X-ray and optical/UV bands are presented correspondingly in Sections 2, 3 and 4. The SED of PKS 0537-286 and its evolution in time is presented in Section 5, and the origin of the emission is discussed in Section 6. The results are presented and discussed in section 7 while the summary is given in Section 8.

## 2 *Fermi*-LAT OBSERVATIONS AND DATA ANALYSES

*Fermi* satellite launched in 2008 carries two instruments- the Large Area Telescope (LAT) is the main instrument on board designed to scan the entire sky in  $\gamma$ -ray band, and the Gamma-ray Burst

Monitor (GBM) is designed to study gamma-ray bursts. LAT is a pair-conversion  $\gamma$ -ray telescope sensitive in the energy range from 20 MeV to 300 GeV with a field of view of  $\sim 2.4$  sr. It is by default in the all sky scanning mode which allows to study the HE properties of various sources, including blazars. For more details on the LAT see [Atwood et al. \(2009\)](#).

We have analyzed the  $\gamma$ -ray data collected between August 4 2008 and September 9 2022 (MET=239557417–686130659). The data was reduced and analyzed following the standard procedures described in the *Fermi*-LAT documentation with *fermitools* version 2.0.8 using P8R3\_SOURCE\_V3 instrument response functions. The events in the energy range from 100 MeV to 300 GeV are selected from a circular region of interest (ROI) of  $12^\circ$  radius centered at the  $\gamma$ -ray location of PKS 0537-286 (RA= 89.99, Dec=  $-28.65$ ), retrieving only events classified as *evclass*=128 and *evtype*= 3. A zenith angle cut less than  $90^\circ$  was introduced to remove the secondary  $\gamma$ -rays from the earth limb. The model file that includes point-like sources and background models was created based on the *Fermi*-LAT fourth source catalog (4FGL) incremental version (DR 3; [Abdollahi et al. 2022](#)), which is based on 12 years of initial *Fermi*-LAT operation and includes best-fit spectral parameters of all known 4FGL  $\gamma$ -ray sources in the ROI. The sources which are within  $17^\circ$  from the PKS 0537-286 location were included in the model file; the spectral parameters of the sources within  $12^\circ - 17^\circ$  are fixed to their values reported in 4FGL while they are left free for the sources falling within  $< 12^\circ$  radius. The galactic background and isotropic galactic emissions were modeled with the latest version available files, *gll\_iem\_v07* and *iso\_P8R3\_SOURCE\_V3\_v1*, respectively.

The  $\gamma$ -ray analysis is performed with *gtlike* tool, following the binned likelihood method. Initially, the spectrum of PKS 0537-286 was modeled with a log-parabolic model as in 4FGL. However, the fit was also performed when assuming a power-law model for PKS 0537-286  $\gamma$ -ray emission and the resulting model file was used in the light-curve calculations, because for shorter periods a power-law can be a good approximation of the spectrum. The significance of the source emission is estimated using test statistic (TS), which is defined by  $TS = 2(\ln L_1 - \ln L_0)$  where  $L_1$  and  $L_0$  are maximum likelihoods with and without the source, respectively ([Mattox et al. 1996](#)).

In order to investigate the variability pattern of the source, the light curves were generated by two different methods. Initially, the whole time interval was divided into 5-day intervals and the photon index and flux of PKS 0537-286 were estimated by the unbinned analysis method from *gtlike* tool. Next, in order to obtain a deeper insight into the  $\gamma$ -ray flux evolution in time, the adaptively binned light curve was computed ([Lott et al. 2012](#)). In this method, the bin widths above the optimal energy ( $E_{\text{opt}}$ ) are adjusted to have fixed uncertainty, so in the case of flux increase shorter intervals are estimated, whereas in the quiescent/normal states time bins are wider. This method has been proven to be a powerful tool in finding flaring periods in blazars (e.g., see [Rani et al. 2013](#); [Britto et al. 2016](#); [Sahakyan & Gasparyan 2017](#); [Zargaryan et al. 2017](#); [Baghmalyan et al. 2017](#); [Gasparyan et al. 2018](#); [Sahakyan et al. 2018](#); [Sahakyan 2021](#); [Sahakyan et al. 2022b](#); [Sahakyan & Giommi 2022](#)).

The adaptively binned light curve ( $> E_{\text{opt}} = 168.19$  MeV) is shown in Fig. 1 upper panel. Up to MJD 57740 the  $\gamma$ -ray flux was in its average level of  $(1 - 3) \times 10^{-8}$  photon  $\text{cm}^{-2} \text{s}^{-1}$  with no significant changes, while then, in several occasions, the  $\gamma$ -ray flux increased substantially. The light curve with 5-day ( $> 100$  MeV) and adaptive bins ( $> E_{\text{opt}} = 168.19$  MeV) for the period when the source was active in the  $\gamma$ -ray band are shown correspondingly in Fig. 1 panels a) and b). The first flaring period was

between MJD 57876-57883 when the flux increased with a maximum of  $(5.26 \pm 1.13) \times 10^{-7}$  photon  $\text{cm}^{-2} \text{s}^{-1}$ . Starting from MJD 59170, the source entered an active emission state with several bright flaring periods between MJD 59204-59233, MJD 59301-59411 and MJD 59721-59738. The maximum  $\gamma$ -ray flux of the source,  $(6.32 \pm 1.11) \times 10^{-7}$  photon  $\text{cm}^{-2} \text{s}^{-1}$  was also observed in these  $\gamma$ -ray flaring periods.

Fig. 1 panel c shows the  $\gamma$ -ray photon index estimated for the adaptively binned periods; it varies in time as well. In the non-flaring periods, the  $\gamma$ -ray spectrum is characterised by a soft spectrum with a mean of  $\Gamma \approx 2.83$  but the photon index hardens during the bright periods as can be seen from Fig. 1 panel c. For example, during the first flare between MJD 57876-57883 the hardest index of  $2.49 \pm 0.23$  was observed on MJD 57879.9 or during the second flare between MJD 59204-59233 the hardest index was  $2.25 \pm 0.21$  when the source was in an active state with a flux of  $(6.12 \pm 1.22) \times 10^{-7}$  photon  $\text{cm}^{-2} \text{s}^{-1}$ . During the hardest  $\gamma$ -ray emission period,  $2.23 \pm 0.18$  was detected on MJD 59322 which is unusual for this source.

### 3 NUSTAR DATA ANALYSIS

NuSTAR is a hard X-ray telescope sensitive in the 3-79 keV energy range ([Harrison et al. 2013](#)). NuSTAR with two focal plane modules (FPMs), FPMA and FPMB, observed PKS 0537-286 on 28 December 2020 (MJD 59211.99) and on 24 October 2020 (MJD 59146.17) for 97.1 ks and 24.3 ks, respectively. It should be noted that around these observations PKS 0537-286 was also monitored with Swift (see dashed blue lines in Fig. 1 panel d), so the X-ray spectrum of the source can be obtained in a large range of 0.3-79 keV.

The NuSTAR data was analyzed applying the standard procedure and using *NuSTAR\_Spectra* tool developed in [Middei et al. \(2022\)](#). *NuSTAR\_Spectra* script downloads calibrated and filtered event files from the SSCD repository, uses *XIMAGE* package to precisely locate the source's coordinate then extracts high-level scientific products for the detected sources using *nuproducts* routine. The script automatically sets the source extraction region radius depending on the source counts (usually in the range of 30-70 arcsec). The background is computed in an annulus centered on the source with a minimum separation of 50 arcsec between the inner and outer radii. Then, a spectral analysis is performed using the XSPEC package ([Arnaud 1996](#)) adopting Cash statistics ([Cash 1979](#)). More details on *NuSTAR\_Spectra* are available in [Middei et al. \(2022\)](#).

The analysis shows that the X-ray photon index of PKS 0537-286 is the same in both observations -  $1.26 \pm 0.06$  and  $1.26 \pm 0.02$  on MJD 59146.17 and MJD 59211.99, respectively. The X-ray flux between 3-10 keV measured on MJD 59146.17 is  $F_{3-10 \text{ keV}} = (2.72 \pm 0.06) \times 10^{-12}$  erg  $\text{cm}^{-2} \text{s}^{-1}$  and on MJD 59211.99, it increased by about a factor of two,  $F_{3-10 \text{ keV}} = (5.10 \pm 0.04) \times 10^{-12}$  erg  $\text{cm}^{-2} \text{s}^{-1}$ . Similarly, the flux between 10-30 keV also increased in these two observations, being correspondingly  $F_{10-30 \text{ keV}} = (5.79 \pm 0.20) \times 10^{-12}$  erg  $\text{cm}^{-2} \text{s}^{-1}$  and  $F_{10-30 \text{ keV}} = (1.08 \pm 0.01) \times 10^{-11}$  erg  $\text{cm}^{-2} \text{s}^{-1}$ . This shows that the source in the 3.0-30 keV range was in an enhanced state on 28 December 2020.

### 4 SWIFT DATA ANALYSIS

Swift is a space-based observatory with three main instruments on-board, namely burst alert telescope (BAT) sensitive in the energy

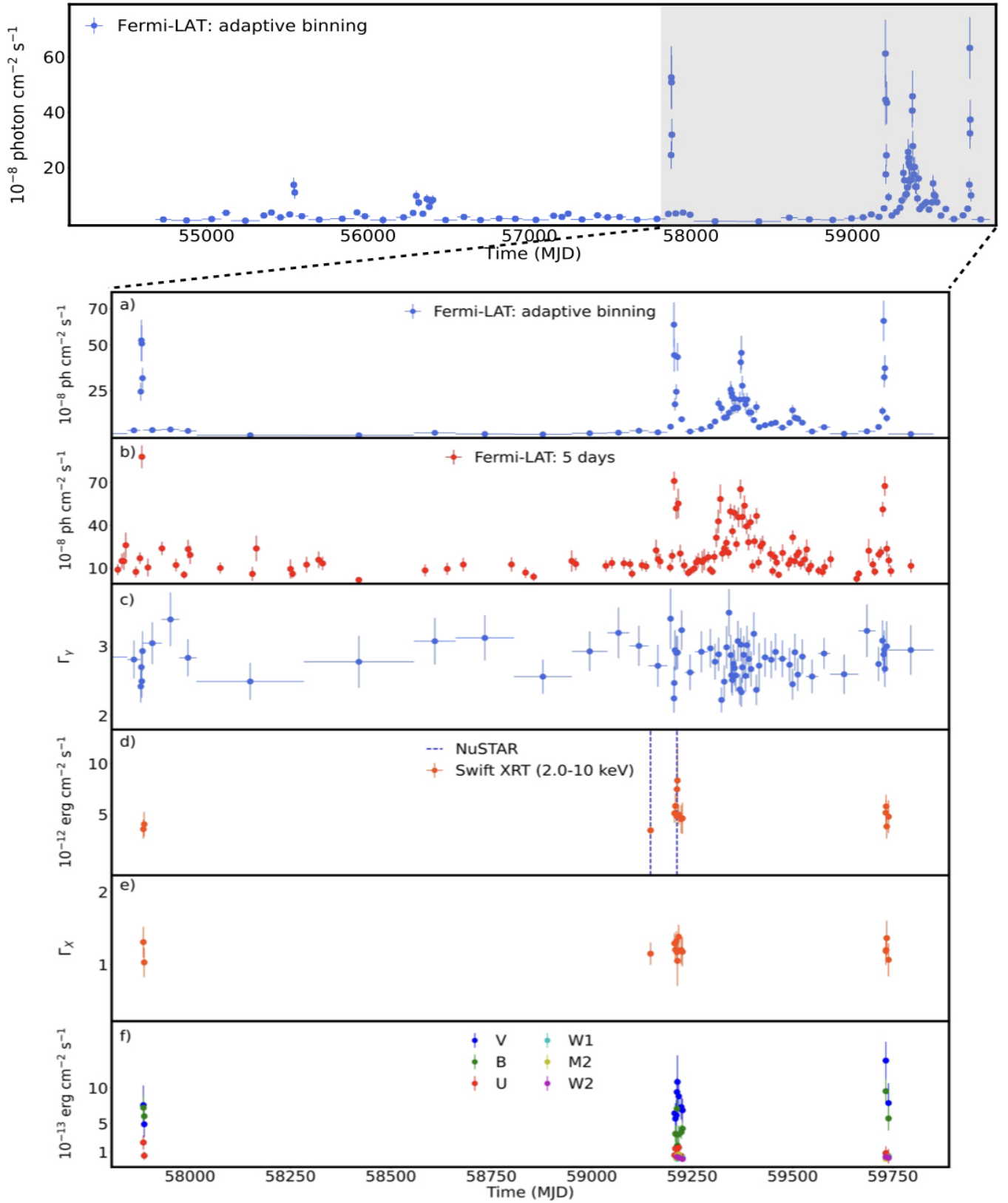


**Figure 1.** Multiwavelength light curve of PKS 0537-286. Top panel shows the long-term adaptively binned  $\gamma$ -ray light curve above 168.19 MeV. The other panels show the light curves after MJD 57800 (16 February 2017) when the source was active in the  $\gamma$ -ray band. *a)* adaptively binned  $\gamma$ -ray light curve, *b)* 5-day binned  $\gamma$ -ray light curve ( $> 100$  MeV), *c)*  $\gamma$ -ray photon index measured for the adaptive time bins, *d)* and *e)* X-ray flux (2-10 keV) and photon index in different Swift observations. The dashed blue lines show the NuSTAR observation times. *f)* Swift UVOT fluxes in V, B, U, W1, M2, and W2 bands.



range of 3.0-150.0 keV, XRT sensitive in the energy range of 0.3-10.0 keV, and UVOT sensitive in the optical/UV band 170 - 650 nm (Gehrels et al. 2004). Swift performed 29 observations of PKS 0537-286 among which nine observations were performed before the launch of *Fermi*-LAT. However, in order to investigate the flux changes in different years, we have analyzed all the data from Swift observations of PKS 0537-286.

#### 4.1 Swift XRT

All the XRT observations were processed with *Swift\_xrtproc* tool applying standard analysis procedure (Giommi et al. 2021). *Swift\_xrtproc* downloads the raw data for each snapshot and for the whole observation, generates exposure maps and calibrated data product using the XRTPIPELINE task adopting standard parameters and filtering criteria. The source region counts are estimated from a circle of a radius of 20 pixels while the background counts from an annular region centred around the source with a radius sufficiently large to avoid contamination from source photons. The resultant ungrouped data is loaded in XSPEC (Arnaud 1996) for spectral fitting using Cash statistics (Cash 1979), modeling the source spectrum as power-law and log-parabola. As a result, the X-ray photon index in the energy range 0.3-10 keV and the flux in various bands are estimated.

The 2-10 keV X-ray flux variation is shown in Fig. 1 panel d). Although in the X-ray band there is a limited number of observations, the flux variation is evident. The X-ray emission of the source in the 2.0-10 keV band was at the level of  $\sim 3.0 \times 10^{-12} \text{ erg cm}^{-2} \text{ s}^{-1}$  but during the bright periods it is  $\geq 5.0 \times 10^{-12} \text{ erg cm}^{-2} \text{ s}^{-1}$ . The highest X-ray flux of  $(8.34 \pm 3.59) \times 10^{-12} \text{ erg cm}^{-2} \text{ s}^{-1}$  was observed on MJD 59213.18. The X-ray spectrum of the source is hard (Fig. 1 panel e) and during all the observations  $\Gamma_{\text{X-ray}} \leq 1.38$ . Therefore, as it is typical for FSRQs, the X-ray band defines the rising part of the second component in the SED.

#### 4.2 Swift UVOT

In the same periods, UVOT observed PKS 0537-286 in V (500-600 nm), B (380- 500 nm), U (300- 400 nm), W1 (220-400 nm), M2 (200-280 nm) and W2 (180-260 nm) filters. All the available 28 observations were downloaded and reduced using HEASoft version 6.29 with the latest release of HEASARC CALDB. Photometry was computed using a five-arcsecond source region centered on the sky position of PKS 0537-286 and the background counts are estimated from a twenty-arcsecond region away from the source. The magnitudes were derived using *uvotsource* tool, then the fluxes were obtained using the conversion factors provided by Poole et al. (2008) which were corrected for extinction using the reddening coefficient  $E(B - V)$  from the Infrared Science Archive<sup>1</sup>.

Fig. 1 panel f) shows the light curve of PKS 0537-286 in optical/UV bands. The source is relatively faint in all the filters with the flux around  $\approx 10^{-13} \text{ erg cm}^{-2} \text{ s}^{-1}$ . In some cases, coinciding with the flares in the  $\gamma$ -ray band, the flux increased several times. The highest flux of the source was observed in V-band; on MJD 59213.18 and MJD 59732.67 it was  $(1.08 \pm 0.37) \times 10^{-12} \text{ erg cm}^{-2} \text{ s}^{-1}$  and  $(1.38 \pm 0.26) \times 10^{-12} \text{ erg cm}^{-2} \text{ s}^{-1}$ , respectively. In addition, VOU-Blazar tool, which allows to search and collect all spectral information accessible through virtual observatory services and build the multiwavelength SEDs of blazars (Chang et al. 2020) was used to

investigate the source emission properties in the infrared band. In particular, data extracted from the Wide-field Infrared Survey Explorer (WISE) and NEOWISE surveys (Mainzer et al. 2014) show that the source emission at 3.4 and 4.6  $\mu\text{m}$  wavelengths (infrared) was at the level of several times  $10^{-13} \text{ erg cm}^{-2} \text{ s}^{-1}$ .

### 5 MULTIWAVELENGTH SEDS

The data analyzed in this paper allows to build the SEDs of PKS 0537-286 in different periods. The single snapshot SED provides substantial information on the source emission properties whereas the variation of these SEDs in time is crucial for understanding the dynamical changes in the emission components. For this purpose, we generated SED/Light curve animation of PKS 0537-286 by showing the  $\gamma$ -ray spectra with all available data sets. For each adaptively binned interval we performed  $\gamma$ -ray spectral analysis using the unbinned likelihood method implemented in *gtlike* tool. Then, for each  $\gamma$ -ray period, together with the  $\gamma$ -ray data we plotted the Swift XRT, NuSTAR and Swift UVOT data as well as archival data extracted with VOU-blazar tool. By going from one to another  $\gamma$ -ray period we can investigate the changes in the multiwavelength SED of PKS 0537-286.

The SED/light curve animation is available here [youtube.com/4UPqf-C7EWc](https://www.youtube.com/watch?v=4UPqf-C7EWc). As the blazar is at  $z = 3.10$  the UVOT flux could be affected by absorption of neutral hydrogen in intervening Lyman- $\alpha$  absorption systems (e.g., Ghisellini et al. 2011) which was corrected using the attenuation calculated in Ghisellini et al. (2010) for the UVOT filters. The SED/light curve animation shows the high amplitude changes observed in the  $\gamma$ -ray band; the gray background data points show the  $\gamma$ -ray flux estimated in different periods. Also, the spectral hardening in several bright  $\gamma$ -ray periods can be seen.

### 6 ORIGIN OF BROADBAND EMISSION

In the previous section, the generated multiwavelength SEDs show the features of PKS 0537-286 emission in different periods. It is especially important to investigate the processes taking place in the jet of high redshift blazars as they could provide information on the jet plasma state in the early Universe. For this reason, the following periods were considered for modeling:

- The SED between MJD 55150-55330 when the source was in the quiescent state, i.e., the  $\gamma$ -ray flux above 100 MeV was  $(2.77 \pm 0.84) \times 10^{-8} \text{ photon cm}^{-2} \text{ s}^{-1}$  and the 2-10 keV X-ray flux was  $(3.29 \pm 1.11) \times 10^{-12} \text{ erg cm}^{-2} \text{ s}^{-1}$ .
- The SED between MJD 59208-59212 when the source was bright in the  $\gamma$ -ray and X-ray (2-10 keV) bands with corresponding fluxes of  $(5.46 \pm 0.83) \times 10^{-8} \text{ photon cm}^{-2} \text{ s}^{-1}$  and  $(7.47 \pm 1.18) \times 10^{-12} \text{ erg cm}^{-2} \text{ s}^{-1}$ . This period coincides with the NuSTAR observation on MJD 59211.99 which showed that the source was in an elevated X-ray emission state also in the 3-30 keV range.

The broadband SEDs were modeled using a one-zone leptonic scenario. In this model, it is assumed that the emission originates from a spherical blob of radius  $R$  moving with a bulk Lorentz factor of  $\Gamma$  at a small inclination angle of  $\theta$  with respect to the observer. Due to the relativistic motion and small  $\theta$  the radiation will be Doppler amplified by a factor of  $\delta \approx \Gamma$ . The emission region magnetized with a field strength of  $B$  is filled with relativistic electrons whose energy distribution is given by

$$N_e = N_0 \gamma^{-p} \exp\left(-\frac{\gamma}{\gamma_{\text{cut}}}\right) \quad \gamma > \gamma_{\text{min}} \quad (1)$$

<sup>1</sup> <http://irsa.ipac.caltech.edu/applications/DUST/>

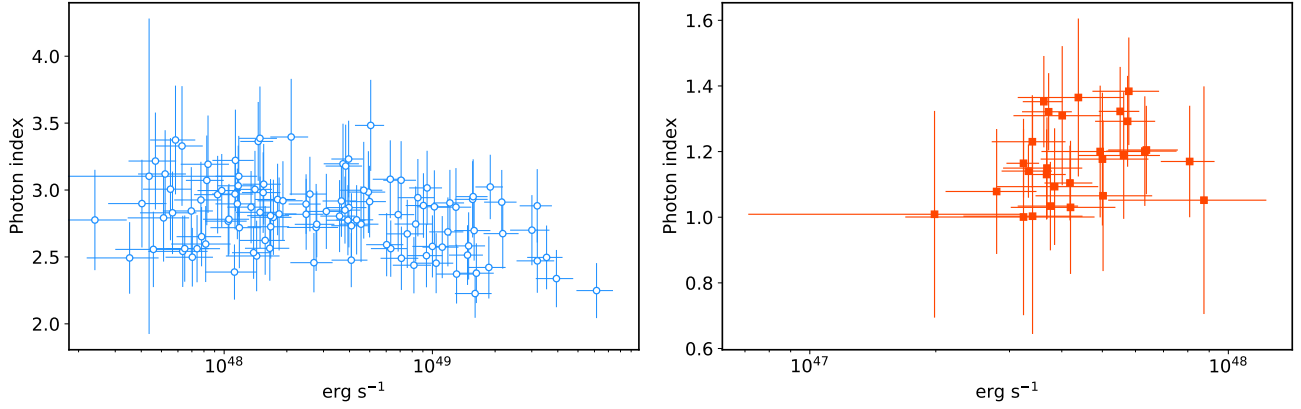


**Figure 2.** The luminosity versus the spectral index in the  $\gamma$ -ray (left panel) and X-ray bands (right panel).

where  $\gamma = E_e/m_e c^2$  is the electron Lorentz factor,  $p$  is the power-law index,  $\gamma_{\min}$  and  $\gamma_{\text{cut}}$  are the minimum and cut-off energy, respectively. The parameter  $N_0$  defines the electron energy density through  $U_e = m_e c^2 \int \gamma N_e(\gamma) d\gamma$ .

The electrons with energy distribution given by Eq. 1 undergo synchrotron losses under the magnetic field, producing the data observed between radio to X-ray bands. Instead, the second component in the SED, from X-rays to  $\gamma$ -rays, is from the inverse Compton scattering of internal and external photons on the same population of the electrons. When the electrons upscatter the synchrotron photons, the second component is explained by the SSC component (Ghisellini et al. 1985; Maraschi et al. 1992; Bloom & Marscher 1996). Alternatively, if the emission region is within the BLR, the second component can be due to external Compton scattering of direct disk radiation (EIC-disk; Dermer et al. 1992; Dermer & Schlickeiser 1994) and/or due to external Compton scattering of photon reflected from BLR clouds (EIC-BLR; Sikora et al. 1994). Instead, if the jet energy dissipation occurs at larger distances it can be due to external Compton scattering of dusty torus photons (EIC-torus; Błażejowski et al. 2000).

In this paper, for a general view we consider three different scenarios: *i*) the broadband emission from PKS 0537-286 is entirely due to synchrotron/SSC radiation, *ii*) the jet dissipation region is close to the central black hole, and SSC, EIC-disk and EIC-BLR are contributing to the HE component and *iii*) the emission region is beyond the BLR and the HE component is due to EIC-torus. It is assumed that BLR is a spherical shell (e.g., Donea & Protheroe 2003) with lower and upper boundaries of  $0.9 \times R_{\text{BLR}}$  and  $1.2 \times R_{\text{BLR}}$ , respectively.  $R_{\text{BLR}}$  is assumed to scale as  $R_{\text{BLR}} = 10^{17} L_{\text{disc},45}^{0.5}$  cm where  $L_{\text{disc},45} = L_{\text{disc}}/10^{45} \text{ erg s}^{-1}$  is the accretion disk luminosity (Ghisellini & Tavecchio 2015). Similarly, we assume that the distance of dusty torus is  $2 \times 10^{18} L_{\text{disc},45}^{0.5}$  (Ghisellini & Tavecchio 2015) which emits  $\eta = 0.5$  fraction of disk luminosity in the IR range for which we adopted  $T_{\text{torus}} = 10^3$  K effective temperature. The disk luminosity and effective temperature are correspondingly  $8.7 \times 10^{46} \text{ erg s}^{-1}$  and  $T_{\text{disk}} = 1.9 \times 10^4$  K estimated by fitting the thermal blue-bump component in the SED with a black-body component.

The remaining free model parameters are  $p$ ,  $\gamma_{\min}$ ,  $\gamma_{\text{cut}}$ ,  $U_e$ ,  $B$  and  $R$  which should be constrained during the fitting. The SED fitting is performed using publicly available code JetSet which is a numerical code allowing to fit the radiative models to data and obtain the parameters statistically better explaining them (Massaro et al. 2006; Tramacere et al. 2009, 2011; Tramacere 2020). These

parameters are initially constrained by using the Minuit optimizer and then improved by Markov Chain Monte Carlo (MCMC) sampling of their distributions. We applied the EBL model from Franceschini et al. (2008) to correct the attenuation in the HE  $\gamma$ -ray band, but as the  $\gamma$ -ray data extends to several tens of GeV it affects only the model extrapolation to higher energies.

## 7 RESULTS AND DISCUSSIONS

At  $z = 3.10$ , PKS 0537-286 is one of the most powerful FSRQs in the extragalactic  $\gamma$ -ray sky; the time-averaged  $\gamma$ -ray luminosity of the source is  $1.90 \times 10^{48} \text{ erg s}^{-1}$  (assuming a distance of 27.08 Gpc). However, in several occasions, the source shows bright  $\gamma$ -ray flares when the flux substantially increases and the spectrum hardens. Fig. 2 left panel shows the  $\gamma$ -ray luminosity of PKS 0537-286 versus the photon index. During the bright periods, the luminosity increases, being above  $10^{49} \text{ erg s}^{-1}$ ; the maximum  $\gamma$ -ray luminosity corresponds to  $6.14 \times 10^{49} \text{ erg s}^{-1}$ . It should be noted that among 113 adaptively binned intervals, the source luminosity was above  $10^{49} \text{ erg s}^{-1}$  in 25 intervals amounting 61.8 days when extreme  $\gamma$ -ray luminosity was observed. Photon index hardening with increasing luminosity/flux can be noticed in Fig. 2 left panel. In order to test possible correlation/anti-correlation between the luminosity and photon index, a Pearson correlation test was applied which yielded  $-0.39$  with a probability of  $P = 1.2 \times 10^{-5}$ . This indicates moderate anti-correlation between the luminosity and photon index, that is when the source emission becomes brighter the photon index hardens (harder-when-brighter trend). It should be noted that for blazars such trend is frequently observed in different bands (e.g., Abdo et al. 2010b,d; Baghmanyan et al. 2017; Sahakyan & Giommi 2021; Sahakyan 2021; Gasparyan et al. 2018; Sahakyan & Giommi 2022) which can be interpreted as interplay between acceleration and cooling of the electrons (Kirk et al. 1998).

PKS 0537-286 shows also interesting features in the X-ray band. The X-ray photon index versus the 0.3 – 10 keV X-ray luminosity is shown in Fig. 2 right panel. The X-ray emission is characterized by a hard spectrum ( $\Gamma_{\text{X-ray}} < 1.38$ ) with a high luminosity ( $> 10^{47} \text{ erg s}^{-1}$ ). It should be noted that *XMM-Newton* observations of PKS 0537-286 also showed a high luminosity of  $2 \times 10^{47} \text{ erg s}^{-1}$  with a spectral index of  $1.27 \pm 0.02$  (Reeves et al. 2001). There is no evidence of softening or hardening when the source gets brighter in the X-ray band; the highest luminosity in the X-ray band is  $8.74 \times 10^{47} \text{ erg s}^{-1}$  observed on MJD 59213.18. Similarly, the 3 – 30 keV

X-ray luminosity was  $1.40 \times 10^{48} \text{ erg s}^{-1}$  on MJD 59211.99 and  $7.47 \times 10^{47} \text{ erg s}^{-1}$  on MJD 59146.17.

The SED of PKS 0537-286 was assembled in the flaring and quiescent periods (see Fig. 3). Comparing and contrasting the jet parameters obtained through modeling of the SED in different periods is crucial, allowing to understand the processes at work in the jet of PKS 0537-286.

### 7.1 Synchrotron/SSC emission from the jet

Fig. 3 panels a and b show the results of the modeling when the entire emission is due to synchrotron/SSC emission from a compact region of the jet when the source is in a quiescent and flaring state, respectively. The corresponding model parameters are given in Table 1. In the quiescent state, the SED modeling shows that the spectral slope of the emitting particle distribution is  $1.8 \pm 0.1$  and their distribution extends up to  $(1.2 \pm 0.1) \times 10^4$ . The strength of the magnetic field is found to be  $(9.3 \pm 0.8) \times 10^{-3} \text{ G}$ . The emission region size is  $(2.0 \pm 0.1) \times 10^{17} \text{ cm}$ , which is consistent with the flux variability of  $t_{\text{var}} = (1+z) \times R/c \approx 18.7$  days. The Doppler boosting factor is  $16.8 \pm 1.2$  which is not different from the values usually estimated for FSRQs (e.g., see Ghisellini & Tavecchio 2015). In this case, the synchrotron component decreases at  $< 10^{14} \text{ Hz}$  and it does not take into account the observed optical/UV data which are interpreted as thermal emission from the accretion disk (see the next subsection).

In the flaring period (Fig. 3 panel b), the SED modeling shows that the emitting electrons have a harder spectrum with  $p = 1.6 \pm 0.03$  as compared with that in the quiescent state. The electrons are accelerated up to  $\gamma_{\text{cut}} = (1.1 \pm 0.1) \times 10^4$  which is not significantly different from that in the quiescent state. In the flaring state, the magnetic field also increased,  $B = (1.7 \pm 0.1) \times 10^{-2} \text{ G}$ , which is caused by the increase of the synchrotron flux. Also, the Doppler boosting factor increased from  $16.8 \pm 1.2$  to  $24.9 \pm 1.1$  in order to explain the slight shift of the HE peak towards higher energies; above 100 MeV the  $\gamma$ -ray spectrum in the flaring period has a photon index of  $\Gamma_{\gamma} = 2.73 \pm 0.17$  as compared with that of  $\Gamma_{\gamma} = 2.91 \pm 0.16$  in the quiescent state. The modeling shows that during the flare, the emission is produced from a smaller region with a radius of  $(1.6 \pm 0.1) \times 10^{17} \text{ cm}$  corresponding to  $t_{\text{var}} \approx 10.0$  days, which indicates that the flaring emission is from a compact and faster moving region.

### 7.2 Emitting region within the BLR

Fig. 3 panels c and d show the SED modeling assuming the jet dissipation occurred close to the central source. In this case, the density of disk-emitted and BLR-reflected photons in the jet frame (taking into account Doppler amplification) is comparable with or larger than that of synchrotron photons, so their inverse Compton scattering has a non-negligible contribution. The thermal emission from the accretion disk, modeled as a black body, is shown with a pink dashed line. In the quiescent state (Fig. 3 panel c), the low-energy component of the spectrum (up to  $10^{16} \text{ Hz}$ ) can be reasonably well explained by combined synchrotron and black body components. The data in the X-ray band is mostly dominated by the EIC-disk component (blue dashed line in Fig. 3) with SSC contributing in the soft X-ray band, whereas the emission in the  $\gamma$ -ray band is due to EIC-disk and EIC-BLR components (blue dashed and purple dot-dot-dashed lines in Fig. 3, respectively). As compared with the synchrotron/SSC model, the distribution of the electrons is narrower with  $p = 2.3 \pm 0.2$  and  $\gamma_{\text{cut}} = (0.3 \pm 0.1) \times 10^3$ , because the average energy of the external photons is larger than that of the synchrotron one. The Doppler

boosting factor is  $\delta = 13.4 \pm 1.3$  but the magnetic field is significantly larger,  $B = 3.5 \pm 0.4 \text{ G}$ . Since the flux in the HE band depends on the photon and particle density and the content of external photons is higher (inferred from the observed high Compton dominance, i.e., the ratio between the peak flux of inverse Compton and synchrotron components), the number of emitting electrons is reduced; to produce the synchrotron emission at the same level higher magnetic field is required. The emission is produced in a more compact region with a radius of  $(0.2 \pm 0.02) \times 10^{17} \text{ cm}$ , smaller than  $R_{\text{BLR}} = 9.3 \times 10^{17} \text{ cm}$ .

During the flaring period, in the optical/UV band, the synchrotron emission from the jet dominates over the thermal emission from the accretion disk (Fig. 3 panel d). As the synchrotron emission extends to higher frequencies, the SSC component makes a non-negligible contribution in the X-ray band (orange dot-dashed line in Fig. 3 panel d). The  $\gamma$ -ray emission is mostly due to the EIC-disk component (blue dashed line in Fig. 3 panel d) and EIC-BLR contributes at higher  $\gamma$ -ray energies (purple dot-dot-dashed line in Fig. 3 panel d). In this case, the electron distribution is nearly flat with  $p = 2.2 \pm 0.1$  and extends up to  $(2.5 \pm 0.2) \times 10^3$ . The increase of the energy up to which the electrons are effectively accelerated ( $\gamma_{\text{cut}}$ ) resulted in the shift of the synchrotron component to higher frequencies and domination over the disk thermal emission. The Doppler boosting is  $\delta = 11.4 \pm 0.7$ , the magnetic field is  $B = 3.0 \pm 0.2 \text{ G}$  and the emission region radius is  $(0.1 \pm 0.01) \times 10^{17} \text{ cm}$ . This is smaller than that estimated in the quiescent state and corresponds to 1.5 days variability.

### 7.3 Emitting region outside BLR

Fig. 3 panels e and f show PKS 0537-286 SED modeling assuming the emission region is beyond the BLR. In the quiescent state, the HE component is entirely dominated by EIC-torus (yellow dot-dot-dashed line in Fig. 3 panel e) and SSC contributing in the soft X-ray band (orange dot-dashed line in Fig. 3 panel e). In the flaring state, the peak of the SSC component is around  $\sim 10^{22} \text{ Hz}$  (orange dot-dashed line in Fig. 3 panel f) making a non-negligible contribution to the X-ray band, but again, the HE  $\gamma$ -ray data is solely explained by the EIC-torus component (yellow dot-dot-dashed line in Fig. 3 panel f). The model parameters given in Table 1 show that in the quiescent and flaring states the electron distribution has a similar power-law index  $p \approx 2.4$ , but in the flaring state the cut-off energy is larger,  $\gamma_{\text{cut}} = (6.7 \pm 0.7) \times 10^3$  as compared to  $\gamma_{\text{cut}} = (1.3 \pm 0.1) \times 10^3$ . This is because *i*) the synchrotron component should extend beyond the optical/UV band and *ii*) during the flare the  $\gamma$ -ray spectrum is harder, shifting this component towards higher frequencies. Also, the modeling shows that the Doppler boosting and magnetic field do not substantially change, correspondingly being  $\delta = 15.3 \pm 0.7$  and  $B = 0.2 \pm 0.01 \text{ G}$  and  $\delta = 14.2 \pm 1.0$  and  $B = 0.2 \pm 0.02 \text{ G}$  for the flaring and quiescent states. However, again in the flaring state, the emission region has a slightly smaller radius  $(1.4 \pm 0.1) \times 10^{17} \text{ cm}$  as compared with  $(2.0 \pm 0.1) \times 10^{17} \text{ cm}$ .

### 7.4 Jet luminosity

The parameters estimated during the modeling are used to compute the jet luminosity. The jet power carried by the electrons, calculated as  $L_e = \pi c R_b^2 \Gamma^2 U_e$ , and by magnetic field, calculated as  $L_B = \pi c R_b^2 \Gamma^2 U_B$ , are given in Table 1. In the case of synchrotron/SSC scenario (Fig. 3 panels a and b), the jet should be strongly particle dominated with a luminosity of the order of  $\approx 10^{47} \text{ erg s}^{-1}$  where the

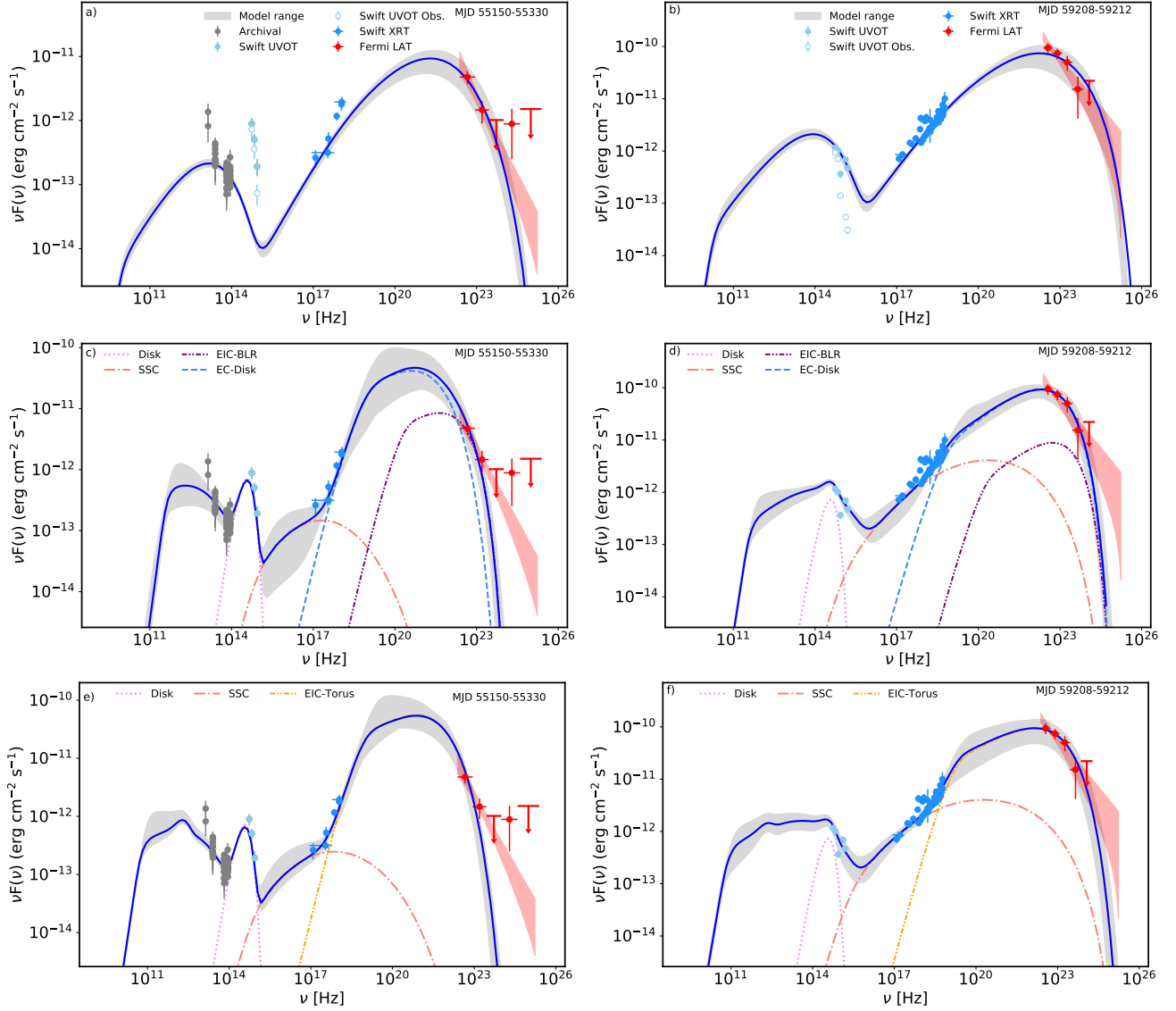


**Figure 3.** The broadband SEDs of PKS 0537-286 in the quiescent (left panels) and flaring (right panels) states. Panels a and b correspond to SED modeling when the emission is entirely due to synchrotron/SSC radiation. The SED modeling when the emission region is within the BLR is shown in panels c and d, while in panels e and f it is outside the BLR. The blue solid curve shows the sum of all components and the gray shaded area is the uncertainty region from MCMC sampling of the parameters. The color code of the other components is given in the legends. In panels a and b, the observed and absorption-corrected Swift UVOT fluxes are shown with empty and filled light blue circles, respectively.

**Table 1.** Parameters best describing the PKS 0537-286 multiwavelength emission in the scenarios shown in Fig. 3.

	SSC		EIC-BLR		EIC Torus	
	quiescent	flare	quiescent	flare	quiescent	flare
$p$	$1.8 \pm 0.1$	$1.6 \pm 0.03$	$2.3 \pm 0.2$	$2.2 \pm 0.1$	$2.4 \pm 0.1$	$2.4 \pm 0.1$
$\gamma_{\text{cut}}/10^3$	$11.8 \pm 0.8$	$11.5 \pm 0.6$	$0.3 \pm 0.1$	$2.5 \pm 0.2$	$1.3 \pm 0.1$	$6.7 \pm 0.7$
$\gamma_{\text{min}}$	$9.5 \pm 1.0$	$1.3 \pm 0.1$	$26.1 \pm 3.8$	$30.1 \pm 2.5$	$65.7 \pm 3.4$	$103.9 \pm 9.0$
$\delta$	$16.8 \pm 1.2$	$24.9 \pm 1.1$	$13.4 \pm 1.3$	$11.4 \pm 0.7$	$15.3 \pm 0.7$	$14.2 \pm 1.0$
$B[\text{G}]$	$(9.3 \pm 0.8) \times 10^{-3}$	$(1.7 \pm 0.1) \times 10^{-2}$	$3.5 \pm 0.4$	$3.0 \pm 0.2$	$0.2 \pm 0.01$	$0.2 \pm 0.02$
$R[\text{cm}]/10^{17}$	$2.0 \pm 0.1$	$1.6 \pm 0.1$	$0.2 \pm 0.02$	$0.1 \pm 0.01$	$2.0 \pm 0.1$	$1.4 \pm 0.1$
$L_e[\text{erg s}^{-1}]$	$1.2 \times 10^{47}$	$1.2 \times 10^{47}$	$1.3 \times 10^{45}$	$2.0 \times 10^{45}$	$1.1 \times 10^{46}$	$1.3 \times 10^{46}$
$L_B[\text{erg s}^{-1}]$	$3.5 \times 10^{42}$	$1.8 \times 10^{43}$	$2.2 \times 10^{45}$	$5.3 \times 10^{44}$	$1.3 \times 10^{45}$	$7.9 \times 10^{44}$



magnetic luminosity has a marginal contribution ( $L_e/L_B \approx 3 \times 10^4$ ). This is natural, given the SED of PKS 0537-286 in both quiescent and flaring periods shows strong Compton dominance. Relatively high luminosity is also estimated in the modeling when the emitting region is outside the BLR;  $L_e + L_B = 1.2 \times 10^{46} \text{ erg s}^{-1}$  with  $L_e/L_B = 8.1$  and  $L_e + L_B = 1.4 \times 10^{46} \text{ erg s}^{-1}$  with  $L_e/L_B \approx 17$  for the quiescent and flaring states, respectively. When the emitting region is within the BLR, a lower jet luminosity is required,  $L_e + L_B = 6.3 \times 10^{45} \text{ erg s}^{-1}$  and  $L_e + L_B = 2.5 \times 10^{45} \text{ erg s}^{-1}$  for the quiescent and flaring states, respectively, and the system is close to equipartition with  $L_e/L_B = 0.5$  and  $L_e/L_B = 3.7$  for the quiescent and flaring states, respectively.

Also, the total kinetic energy of the jet, defined as  $L_{\text{kin}} = L_e + L_B + L_{\text{p,cold}}$ , can be evaluated. Assuming a proton-to-electron comoving number density ratio of  $N_p/N_e \approx 0.1$ , in the most energy demanding model (synchrotron/SSC)  $L_{\text{kin}} = 3.2 \times 10^{47} \text{ erg s}^{-1}$  and  $L_{\text{kin}} = 4.4 \times 10^{47} \text{ erg s}^{-1}$  are estimated for the quiescent and flaring states, respectively. In the most optimistic scenario (EIC-BLR),  $L_{\text{kin}} = 1.1 \times 10^{46} \text{ erg s}^{-1}$  and  $L_{\text{kin}} = 6.0 \times 10^{45} \text{ erg s}^{-1}$  for the quiescent and flaring states, respectively. In this case, even if assuming  $N_p/N_e \approx 1$ , one would obtain  $L_{\text{kin}} = 4.8 \times 10^{46} \text{ erg s}^{-1}$  and  $L_{\text{kin}} = 3.8 \times 10^{46} \text{ erg s}^{-1}$  for the quiescent and flaring states, respectively. It is interesting that this luminosity is still lower than the disk luminosity estimated from the optical/UV data fitting. However, considering that the presence of the pairs can reduce the jet power (e.g., Pjanka et al. 2017), the estimated jet luminosity will be by several factors lower than the accretion disk luminosity.

In Bottacini et al. (2010), the broadband SED of PKS 0537-286 was modeled assuming the particles are injected into the emitting region, which is inside the BLR, and interact with the internal and external photon fields. The disk luminosity was estimated to be  $1.7 \times 10^{47} \text{ erg s}^{-1}$  and  $8.4 \times 10^{46} \text{ erg s}^{-1}$  by fitting the data observed in 2008 and 2006, respectively; the latter value is similar to the disk luminosity estimated in the current study. Their modeling showed that  $L_e$  is in the range of  $(2.5 - 4.0) \times 10^{46} \text{ erg s}^{-1}$  and  $L_B$  in  $(1.0 - 2.0) \times 10^{45} \text{ erg s}^{-1}$ .  $L_e$  is slightly larger than that estimated in the current study (see Table 1) which is related with different assumptions made in the modelings (e.g., emitting region radius, Doppler boosting factor, etc.).

## 8 SUMMARY

In this work, we have performed a broadband study of the high redshift blazar PKS 0537-286. The main findings are summarized as follows:

- PKS 0537-286 is among the highest redshift blazars detected by *Fermi*-LAT. Its  $\gamma$ -ray emission, monitored since 2008, appeared relatively constant until 2017, then multiple powerful  $\gamma$ -ray flares were observed. Starting from MJD 59170, the source was in an enhanced  $\gamma$ -ray emission state when the  $\gamma$ -ray luminosity reached  $6.14 \times 10^{49} \text{ erg s}^{-1}$ . During the considered fourteen years, the  $\gamma$ -ray luminosity of the source exceeded  $10^{49} \text{ erg s}^{-1}$  for 61.8 days in total.
- The  $\gamma$ -ray photon index of the source varies as well. The mean of the  $\gamma$ -ray photon index during non flaring periods is  $\approx 2.83$  which substantially hardens during the flares: the hardest index of  $2.23 \pm 0.18$  was observed on MJD 59322. There is a moderate anti-correlation between the  $\gamma$ -ray photon index and luminosity.
- The source is very luminous in the X-ray band with a  $0.3 - 10 \text{ keV}$  luminosity between  $10^{47} - 10^{48} \text{ erg s}^{-1}$  and with a hard spectrum ( $\Gamma_{\text{X-ray}} < 1.38$ ). The available NuSTAR observations show that the

hard X-ray spectrum extends up to  $30 \text{ keV}$  with  $\Gamma_{\text{X-ray}} = 1.26$  with a luminosity between  $(0.75 - 1.40) \times 10^{48} \text{ erg s}^{-1}$ .

- In order to understand the underlying physical processes at work in the jet of PKS 0537-286, the SEDs during the quiescent and flaring states were reproduced using a simple one-zone leptonic emission model considering different locations of the emission region. In the quiescent state, the combined synchrotron and thermal accretion disk components can explain the IR-optical-UV data, whereas X-ray to HE  $\gamma$ -ray data are due to inverse-Compton scattering of the disk and BLR-reflected photons. Instead, in the flaring state, the jet synchrotron emission dominates in the optical/UV band and the X-ray to HE  $\gamma$ -ray emission is due to combination of SSC, EIC-disk and EIC-BLR components. The modeling in the quiescent to flaring states showed that the flare was caused by the electron distribution changes, i.e., the electron power-law index hardened to  $p = 2.2 \pm 0.1$  and the cut-off energy was  $\gamma_{\text{cut}} = (2.5 \pm 0.2) \times 10^3$ .

- From the required jet energy point of view, the model with the emission region within the BLR is preferred. During the flaring event, the emitting region is nearly in equipartition with  $L_e/L_B = 3.7$  and the jet total luminosity is  $L_{\text{tot}} = 3.8 \times 10^{46} \text{ erg s}^{-1}$  when assuming a proton-to-electron comoving number density ratio of  $N_p/N_e \approx 1$ . This luminosity is slightly lower than the accretion disk luminosity of  $L_{\text{disc}} = 8.7 \times 10^{46} \text{ erg s}^{-1}$  estimated through fitting of UV/optical data.

Among the high red-shift blazars, PKS 0537-286 is exceptional, having a reach multiwavelength data set (especially in the X-ray and  $\gamma$ -ray bands) which allows to investigate the processes taking place in the jet. Further multiwavelength monitoring of such distant and powerful sources will improve our understanding of the radiative processes at work in the relativistic jets in the early Universe.

## ACKNOWLEDGEMENTS

We acknowledge the use of data, analysis tools and services from the Open Universe platform, the ASI Space Science Data Center (SSDC), the Astrophysics Science Archive Research Center (HEASARC), the Fermi Science Tools, the Astrophysics Data System (ADS), and the National Extra-galactic Database (NED).

This work was supported by the Science Committee of the Republic of Armenia, in the frames of the research project No 21T-1C260.

This work used resources from the ASNET cloud.

## DATA AVAILABILITY

All the data used in this paper is public and available from the Swift, Fermi and NuSTAR archives. The *Fermi*-LAT, Swift XRT/UVOT and NuSTAR data analyzed in this paper can be shared on a reasonable request to the corresponding author.

## REFERENCES

- Abdo A. A., et al., 2010a, *Phys. Rev. Lett.*, **104**, 101101
- Abdo A. A., et al., 2010b, *ApJ*, **710**, 810
- Abdo A. A., et al., 2010c, *ApJ*, **716**, 30
- Abdo A. A., et al., 2010d, *ApJ*, **721**, 1425
- Abdollahi S., et al., 2022, *ApJS*, **260**, 53
- Ackermann M., et al., 2016, *ApJ*, **824**, L20
- Ackermann M., et al., 2017, *ApJ*, **837**, L5
- Aleksić J., et al., 2014, *Science*, **346**, 1080
- Angioni R., 2020, The Astronomer's Telegram, **14285**, 1

- Ansoldi S., et al., 2018, *ApJ*, **863**, L10
- Arlen T., et al., 2013, *ApJ*, **762**, 92
- Arnaud K. A., 1996, in Jacoby G. H., Barnes J., eds, *Astronomical Society of the Pacific Conference Series Vol. 101, Astronomical Data Analysis Software and Systems V* p. 17
- Atwood W. B., et al., 2009, *ApJ*, **697**, 1071
- Baghmanyan V., Gasparyan S., Sahakyan N., 2017, *ApJ*, **848**, 111
- Biteau J., et al., 2020, *Nature Astronomy*, **4**, 124
- Blażejowski M., Sikora M., Moderski R., Madejski G. M., 2000, *ApJ*, **545**, 107
- Bloom S. D., Marscher A. P., 1996, *ApJ*, **461**, 367
- Bottacini E., et al., 2010, *A&A*, **509**, A69
- Böttcher M., Reimer A., Sweeney K., Prakash A., 2013, *ApJ*, **768**, 54
- Britto R. J., Bottacini E., Lott B., Razzaque S., Buson S., 2016, *ApJ*, **830**, 162
- Capri M., Matsuoka M., Comastri A., Brinkmann W., Elvis M., Palumbo G. G. C., Vignali C., 1997, *ApJ*, **478**, 492
- Cash W., 1979, *ApJ*, **228**, 939
- Cerruti M., Zech A., Boisson C., Emery G., Inoue S., Lenain J.-P., 2019, *MNRAS*, **483**, L12
- Chang Y. L., Brandt C. H., Giommi P., 2020, *Astronomy and Computing*, **30**, 100350
- Cheung C. C., 2017, *The Astronomer's Telegram*, **10356**, 1
- Costamante L., et al., 2001, *A&A*, **371**, 512
- Dermer C. D., Schlickeiser R., 1994, *ApJS*, **90**, 945
- Dermer C. D., Schlickeiser R., Mastichiadis A., 1992, *A&A*, **256**, L27
- Donea A.-C., Protheroe R. J., 2003, *Astroparticle Physics*, **18**, 377
- Fiore F., Elvis M., Giommi P., Padovani P., 1998, *ApJ*, **492**, 79
- Franceschini A., Rodighiero G., Vaccari M., 2008, *A&A*, **487**, 837
- Gao S., Fedynitch A., Winter W., Pohl M., 2019, *Nature Astronomy*, **3**, 88
- Gasparyan S., Sahakyan N., Baghmanyan V., Zargaryan D., 2018, *ApJ*, **863**, 114
- Gasparyan S., Bégué D., Sahakyan N., 2022, *MNRAS*, **509**, 2102
- Gehrels N., et al., 2004, *ApJ*, **611**, 1005
- Ghisellini G., Tavecchio F., 2015, *MNRAS*, **448**, 1060
- Ghisellini G., Maraschi L., Treves A., 1985, *A&A*, **146**, 204
- Ghisellini G., Foschini L., Volonteri M., Ghirlanda G., Haardt F., Burlon D., Tavecchio F., 2009, *MNRAS*, **399**, L24
- Ghisellini G., et al., 2010, *MNRAS*, **405**, 387
- Ghisellini G., et al., 2011, *MNRAS*, **411**, 901
- Giommi P., Menna M. T., Padovani P., 1999, *MNRAS*, **310**, 465
- Giommi P., et al., 2021, *MNRAS*, **507**, 5690
- Harrison F. A., et al., 2013, *ApJ*, **770**, 103
- IceCube Collaboration et al., 2018a, *Science*, **361**, 147
- IceCube Collaboration et al., 2018b, *Science*, **361**, eaat1378
- Keivani A., et al., 2018, *ApJ*, **864**, 84
- Kirk J. G., Rieger F. M., Mastichiadis A., 1998, *A&A*, **333**, 452
- Kneiske T. M., Bretz T., Mannheim K., Hartmann D. H., 2004, *A&A*, **413**, 807
- Li S., Xia Z.-Q., Liang Y.-F., Liao N.-H., Fan Y.-Z., 2018, *ApJ*, **853**, 159
- Lott B., Escande L., Larsson S., Ballet J., 2012, *A&A*, **544**, A6
- Mainzer A., et al., 2014, *ApJ*, **792**, 30
- Mannheim K., 1993, *A&A*, **269**, 67
- Mannheim K., Biermann P. L., 1989, *A&A*, **221**, 111
- Maraschi L., Ghisellini G., Celotti A., 1992, *ApJ*, **397**, L5
- Marcotulli L., et al., 2017, *ApJ*, **839**, 96
- Massaro E., Tramacere A., Perri M., Giommi P., Tosti G., 2006, *A&A*, **448**, 861
- Mattox J. R., et al., 1996, *ApJ*, **461**, 396
- Mazin D., Raue M., 2007, *A&A*, **471**, 439
- Meyer M., Scargle J. D., Blandford R. D., 2019, *ApJ*, **877**, 39
- Middei R., Giommi P., Perri M., Turriziani S., Sahakyan N., Chang Y. L., Leto C., Verrecchia F., 2022, *MNRAS*, **514**, 3179
- Mücke A., Protheroe R. J., 2001, *Astroparticle Physics*, **15**, 121
- Mücke A., Protheroe R. J., Engel R., Rachen J. P., Stanev T., 2003, *Astroparticle Physics*, **18**, 593
- Murase K., Oikonomou F., Petropoulou M., 2018, *ApJ*, **865**, 124
- Padovani P., Giommi P., 1995, *ApJ*, **444**, 567
- Padovani P., et al., 2017, *A&ARv*, **25**, 2
- Padovani P., Giommi P., Resconi E., Glauch T., Arsioli B., Sahakyan N., Huber M., 2018, *MNRAS*, **480**, 192
- Paliya V. S., 2015, *ApJ*, **804**, 74
- Paliya V. S., Parker M. L., Fabian A. C., Stalin C. S., 2016, *ApJ*, **825**, 74
- Paliya V. S., et al., 2019, *ApJ*, **871**, 211
- Paliya V. S., Ajello M., Cao H. M., Giroletti M., Kaur A., Madejski G., Lott B., Hartmann D., 2020, *ApJ*, **897**, 177
- Peñil P., et al., 2020, *ApJ*, **896**, 134
- Petropoulou M., Mastichiadis A., 2015, *MNRAS*, **447**, 36
- Pian E., et al., 1998, *ApJ*, **492**, L17
- Pjanka P., Zdziarski A. A., Sikora M., 2017, *MNRAS*, **465**, 3506
- Poole T. S., et al., 2008, *MNRAS*, **383**, 627
- Rani B., Lott B., Krichbaum T. P., Fuhrmann L., Zensus J. A., 2013, *A&A*, **557**, A71
- Reeves J. N., et al., 2001, *A&A*, **365**, L116
- Ren H. X., Cerruti M., Sahakyan N., 2022, arXiv e-prints, p. arXiv:2204.13051
- Righi C., Tavecchio F., Pacciani L., 2019, *MNRAS*, **484**, 2067
- Sahakyan N., 2018, *ApJ*, **866**, 109
- Sahakyan N., 2019, *A&A*, **622**, A144
- Sahakyan N., 2020, *MNRAS*, **496**, 5518
- Sahakyan N., 2021, *MNRAS*, **504**, 5074
- Sahakyan N., Gasparyan S., 2017, *MNRAS*, **470**, 2861
- Sahakyan N., Giommi P., 2021, *MNRAS*, **502**, 836
- Sahakyan N., Giommi P., 2022, *MNRAS*, **513**, 4645
- Sahakyan N., Baghmanyan V., Zargaryan D., 2018, *A&A*, **614**, A6
- Sahakyan N., Israyelyan D., Harutyunyan G., 2020a, *Astrophysics*, **63**, 1
- Sahakyan N., Israyelyan D., Harutyunyan G., Khachatryan M., Gasparyan S., 2020b, *MNRAS*, **498**, 2594
- Sahakyan N., Giommi P., Padovani P., Petropoulou M., Bégué D., Boccardi B., Gasparyan S., 2022a, arXiv e-prints, p. arXiv:2204.05060
- Sahakyan N., Israyelyan D., Harutyunyan G., Gasparyan S., Vardanyan V., Khachatryan M., 2022b, *MNRAS*, **517**, 2757
- Shukla A., et al., 2018, *ApJ*, **854**, L26
- Siebert J., Matsuoka M., Brinkmann W., Capri M., Mihara T., Takahashi T., 1996, *A&A*, **307**, 8
- Sikora M., Begelman M. C., Rees M. J., 1994, *ApJ*, **421**, 153
- Tramacere A., 2020, *JetSet: Numerical modeling and SED fitting tool for relativistic jets* (ascl:2009.001)
- Tramacere A., Giommi P., Perri M., Verrecchia F., Tosti G., 2009, *A&A*, **501**, 879
- Tramacere A., Massaro E., Taylor A. M., 2011, *ApJ*, **739**, 66
- Urry C. M., Padovani P., 1995, *PASP*, **107**, 803
- Valverde J., Forman J., 2022, *The Astronomer's Telegram*, **15405**, 1
- Wright A. E., Peterson B. A., Jauncey D. L., Condon J. J., 1978, *ApJ*, **226**, L61
- Zamorani G., et al., 1981, *ApJ*, **245**, 357
- Zargaryan D., Gasparyan S., Baghmanyan V., Sahakyan N., 2017, *A&A*, **608**, A37

This paper has been typeset from a  $\text{\LaTeX}$  file prepared by the author.